Active topolectrical circuits

Tejas Kotwal[a,b,c,1], Fischer Moseley[d,1], Alexander Stegmaier[e], Stefan Imhof[f], Hauke Brand[f], Tobias Kießling[f], Ronny Thomale[e], Henrik Ronellenfitsch[b,g,2], and Jörn Dunkel[b,2]

[a]Department of Mathematics, Indian Institute of Technology Bombay, Mumbai 400076, India; [b]Department of Mathematics, Massachusetts Institute of Technology, Cambridge, MA 02139; [c]Division of Applied Mathematics, Brown University, Providence, RI 02912; [d]Department of Physics, Massachusetts Institute of Technology, Cambridge, MA 02139; [e]Institut für Theoretische Physik und Astrophysik, Universität Würzburg, D-97074 Würzburg, Germany; [f]Physikalisches Institut der Universität Würzburg, Universität Würzburg, D-97074 Würzburg, Germany; and [g]Physics Department, Williams College, Williamstown, MA 01267

Edited by David A. Weitz, Harvard University, Cambridge, MA, and approved July 4, 2021 (received for review April 5, 2021)

The transfer of topological concepts from the quantum world to classical mechanical and electronic systems has opened fundamentally different approaches to protected information transmission and wave guidance. A particularly promising emergent technology is based on recently discovered topolectrical circuits that achieve robust electric signal transduction by mimicking edge currents in quantum Hall systems. In parallel, modern active matter research has shown how autonomous units driven by internal energy reservoirs can spontaneously self-organize into collective coherent dynamics. Here, we unify key ideas from these two previously disparate fields to develop design principles for active topolectrical circuits (ATCs) that can self-excite topologically protected global signal patterns. Realizing autonomous active units through nonlinear Chua diode circuits, we theoretically predict and experimentally confirm the emergence of self-organized protected edge oscillations in one- and two-dimensional ATCs. The close agreement between theory, simulations, and experiments implies that nonlinear ATCs provide a robust and versatile platform for developing high-dimensional autonomous electrical circuits with topologically protected functionalities.

topological electronics | active circuits | autonomous signal propagation | self-organized currents

Information transfer and storage in natural and man-made active systems, from sensory organs (1–3) to the internet, rely on the robust exchange of electrical signals between a large number of autonomous units that balance local energy uptake and dissipation (4, 5). Major advances in the understanding of photonic (6–9), acoustic (10–12), and mechanical (13–16) metamaterials have shown that topological protection (17–24) enables the stabilization and localization of signal propagation in passive and active (25–27) dynamical systems that violate time-reversal and/or other symmetries. Recent studies have successfully applied these ideas to realize topolectrical circuits (28) in the passive linear (29–34) and passive nonlinear (35, 36) regimes. However, despite substantial progress in the development of topological wave guides (37), lasers (38, 39), and transmission lines (40–43), the transfer of these concepts to active (44, 45) nonlinear circuits made from autonomously acting units still poses an unsolved challenge. From a broader perspective, not only does harnessing topological protection in nonlinear active circuits promise a new generation of autonomous devices, but also understanding their design and self-organization principles may offer insights into information storage and processing mechanisms in living systems, which integrate cellular activity, electrical signaling, and nonlinear feedback to coordinate essential biological functions (46, 47).

Exploiting a mathematical analogy with active Brownian particle systems (26), we theoretically develop and experimentally demonstrate general design principles for active topolectrical circuits (ATCs) that achieve self-organized, self-sustained, topologically protected electric current patterns. The main building blocks of ATCs are nonlinear dissipative elements that exhibit an effectively negative resistance over a certain voltage range. Negative resistances can be realized using van der Pol (vdP) circuits (48), tunnel diodes, unijunction transistors, solid-state thyristors (49), or operational amplifiers set as negative impedance converters through current inversion (50), and the design principles described below are applicable to all these systems. Indeed, we expect them to apply to an even broader class of nonlinear systems, as similar dynamics also describe electromagnetic resonators with Kerr-type nonlinearities (51–53).

Results

Theoretical Framework. Active electronic circuits with basic nontopological interactions have been studied previously as models of neuronal networks (48) and solitary signal transport (4, 5). To leading order, the negative resistance elements in an active circuit can be described (4, 5) by a nonlinear Rayleigh-type conductance $R^{-1}(V) = -(\alpha - \gamma V^2)$, where V denotes voltage, and α and γ are positive parameters. A prototypical example is the vdP oscillator circuit with capacitance C and inductance L_{ii}, as shown in Fig. 1*A*. When expressed in terms of the rescaled dimensionless voltage $\hat{V}_i = x_i = \sqrt{3\gamma/\alpha}\, V_i$, the

Significance

Originally discovered in condensed-matter physics, topological protection has become a unifying paradigm for understanding robust localized wave propagation in electronic, optical, acoustic, and even geophysical systems. The excitation of topologically protected waves in passive matter typically requires external forcing in a specific frequency range. Here, we show both theoretically and experimentally that robust topological edge modes can be spontaneously self-excited in active systems made from internally powered subunits. Presenting different realizations of active nonlinear electronic circuits, we demonstrate the emergence of self-organized topological wave patterns, in close agreement with predictions from a generic mathematical model. More broadly, these results can provide guidance for designing autonomous active systems with topologically protected signaling and transmission properties.

Author contributions: R.T., H.R., and J.D. designed research; T. Kotwal, F.M., A.S., S.I., H.B., T. Kießling, and H.R. performed research; T. Kotwal, F.M., A.S., S.I., H.B., T. Kießling, and H.R. analyzed data; and T. Kotwal, F.M., A.S., S.I., H.B., T. Kießling, R.T., H.R., and J.D. wrote the paper.

The authors declare no competing interest.

This article is a PNAS Direct Submission.

[1]T. Kotwal and F.M. contributed equally to this work.

[2]To whom correspondence may be addressed. Email: dunkel@mit.edu or hmr1@williams.edu.

This article contains supporting information online at https://www.pnas.org/lookup/suppl/doi:10.1073/pnas.2106411118/-/DCSupplemental.

Published August 4, 2021.

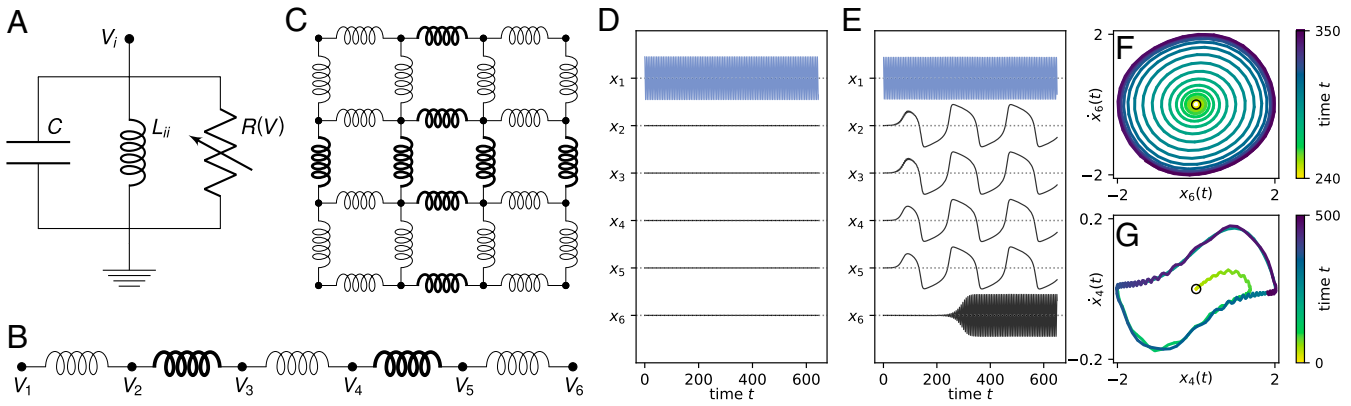

Fig. 1. Schematic and dynamics of active topolectrical SSH circuits. (*A*) Circuit diagram of a basic vdP oscillator with capacitance *C*, inductance L_{ii}, and nonlinear resistor *R*(*V*). (*B* and *C*) One-dimensional and 2D SSH circuits where each node is a vdP oscillator. Thick lines indicate strong coupling *s* and thin lines weak coupling $w \ll s$. (*D*) Oscillator dynamics in an undamped passive ($\varepsilon = 0$) 1D SSH circuit with six nodes. Applying a nonzero initial voltage at the first node, the oscillation remains exponentially localized on that edge. (*E–G*) Dynamics of a 1D ATC ($\varepsilon > 0$) for the same initial condition as in *D*. The high-frequency topological edge mode is activated first and induces slow synchronized bulk oscillations, which eventually actuate the second topological mode at the opposite end. Phase portraits of the boundary (*F*) and bulk (*G*) nodes show the limit cycles of the fast and slow oscillations. The edge oscillators show approximately circular limit cycles typical of weak nonlinearity while the bulk dynamics are of strong relaxation type despite ε being small. Simulation parameters in *D–E*: $g = 1$, $w = 0.003$, $s = g - w$ with $\varepsilon = 0$ in *D* and $\varepsilon = 0.1$ in *E–G*. Initial conditions: $x_1(0) = 2$ and $\dot{x}_1(0) = x_j(0) = \dot{x}_j(0) = 0$ for $j \geq 2$.

dynamics of an isolated vdP-unit i are governed by (54) (*Materials and Methods*)

$$\ddot{x}_i - \varepsilon\left(1 - x_i^2\right)\dot{x}_i + x_i = 0, \qquad [1]$$

where $\varepsilon = \alpha\sqrt{L/C}$, $t = \sqrt{LC}\hat{t}$, and $\dot{x}_i = dx_i/d\hat{t}$. Because this active system is linearly unstable, a stabilizing nonlinearity is necessary to obtain bounded dynamics. In this case, we find limit cycle oscillations (Fig. 1*F*). Eq. **1** is intimately related to that of a harmonically trapped active Brownian particle (55), with position coordinate y and velocity $u = \dot{y}$ described by the standard cubic friction model $\dot{u} = \varepsilon(1 - u^2/3)u - y$. Upon taking the time derivative and identifying $u = \dot{y} = x_i$, one recovers Eq. **1**. It was shown recently (26) that suitably coupled mechanical chains of active Brownian particles can autonomously actuate topological modes. This insight provides guidance for the design of ATCs.

To design an ATC with desired topological properties, we generalize Eq. **1** by introducing suitably chosen couplings between vdP units i and j through inductances L_{ij}; see Fig. 1 *B* and *C* for two examples. Assuming a lattice of vdP units and introducing the symmetric coupling matrix elements $\beta_{ij} = -L_0/L_{ij}$ for $i \neq j$, and $\beta_{ii} = \sum_k L_0/L_{ik}$, Eq. **1** generalizes to

$$\ddot{x}_i - \varepsilon\left(1 - x_i^2\right)\dot{x}_i + \sum_j \beta_{ij} x_j = 0, \qquad [2]$$

where L_0 is the smallest inductance in the circuit.

Interpreting each individual vdP unit as a node in the network graph (Fig. 1 *B* and *C*), the effective dimension d of the ATC can be tuned by increasing the number of couplings. In principle, arbitrary values $d \geq 1$ are realizable with large, densely connected networks (28). For example, for d-dimensional cubic lattices, rows of the coupling matrix $\boldsymbol{\beta} = (\beta_{ij})$ corresponding to bulk nodes will have $2d$ off-diagonal entries. Below, we focus on the cases $d = 1$ (Fig. 1*B*) and $d = 2$ (Fig. 1*C*) to demonstrate the implementation and key properties of ATCs. Generally, through an appropriate choice of $\boldsymbol{\beta}$, it is possible to realize a wide range of topological phases.

One-Dimensional Su–Schrieffer–Heeger ATC: Theoretical Analysis. As a first realization of an ATC, we consider the coupling matrix of a one-dimensional (1D) Su–Schrieffer–Heeger (SSH) model. Originally introduced to describe polyacetylene (56), the SSH model is known to support topologically protected boundary modes in a variety of quantum (57) and classical (16, 26, 28) systems. The $n \times n$ SSH coupling matrix for the case of $n = 6$ vdP units reads (*Materials and Methods*)

$$\boldsymbol{\beta} = \begin{pmatrix} g & -w & 0 & 0 & 0 & 0 \\ -w & g & -s & 0 & 0 & 0 \\ 0 & -s & g & -w & 0 & 0 \\ 0 & 0 & -w & g & -s & 0 \\ 0 & 0 & 0 & -s & g & -w \\ 0 & 0 & 0 & 0 & -w & g \end{pmatrix}, \qquad [3]$$

with the diagonal elements $\beta_{ii} = g > 0$ representing the electrical grounds. In electrical circuits, the diagonal elements of the coupling matrix $\beta_{ii} = \sum_k L_0/L_{ik}$ depend on the neighboring inductors and are generally not uniform. Therefore, we introduce additional ground inductances L_{ii} at all boundaries, such that $\beta_{ii} = g$ is uniform and the coupling matrix represents an instance of the SSH model. Upon generalizing this coupling matrix by permitting nonuniform grounds g_i, one can achieve additional frequency control (*SI Appendix*). The off-diagonal entries $w > 0$ and $s > w > 0$ encode the weak and strong couplings, respectively. Adding more units extends the matrix symmetrically along the diagonal. As in the original quantum SSH model, the strongly coupled nodes form "dimers" that are connected to each other through weak bonds (thin lines in Fig. 1*B*).

To gain intuition about the dynamics of the 1D SSH circuit, it is instructive to first consider the undamped passive topolectrical SSH circuit with $\varepsilon = 0$ and $s \gg w$. In this case, Eqs. **2** and **3** reduce to a linear dynamical system that exhibits topologically protected, exponentially localized modes at both ends of the chain (57). These edge modes have finite frequency for $g > 0$ and become zero modes as $g \to 0$. Their presence can be illustrated by considering an ideal passive ($\varepsilon = 0$) circuit (28) in the almost fully dimerized topological regime ($w \ll s$) with all nodes initially at rest, $x_i(t) = \dot{x}_i(t) = 0$ for $t < 0$. Upon initializing the chain by imposing a nonzero voltage value at the left edge, $x_1(0) > 0$, the boundary node will oscillate with a nonzero amplitude at frequency $\sqrt{g}$, while the amplitudes of the other nodes remain exponentially small (Fig. 1*D*). In the next part, we will see that ATCs with $\varepsilon > 0$ exhibit fundamentally different behaviors that promise a broad range of applications.

Adding just a small amount of activity ($0 < \varepsilon \ll \sqrt{g}$) significantly alters the dynamics of the edge and bulk oscillators (Fig. 1 *E*–*G*). In the topological regime, characterized by $s \gg w$ and $g \geq s + w$, the boundary nodes are only weakly coupled to the bulk and behave similarly to isolated vdP oscillators. The active local energy input renders the rest state ($x_i = \dot{x}_i = 0$) unstable, forcing the boundary nodes to approach a stable limit cycle corresponding to an oscillation at frequency $\sqrt{g}$ (Fig. 1 *E* and *F*). By contrast, bulk nodes are strongly coupled to one or more neighbors, resulting in nontopological, distinct bulk dynamics reminiscent of highly nonlinear relaxation oscillations (Fig. 1 *E* and *G*). For fully decoupled pairs of vdP oscillators, one expects stable phase-locked solutions with relative phase 0 or π (58, 59). Because the system is close to the vdP oscillator's Andronov–Hopf bifurcation (60), the frequencies of the limit cycle are approximately given by the imaginary parts of the Jacobian of the dynamics (Eq. **2**) at the unstable rest state. The Jacobian's eigenvalues are $\lambda_{k,\pm} = \frac{1}{2}(\varepsilon \pm \sqrt{\varepsilon^2 - 4\mu_k}) = \pm\sqrt{-\mu_k} + \mathcal{O}(\varepsilon)$, where μ_k are the eigenvalues of the coupling matrix $\boldsymbol{\beta}$ (*SI Appendix*). This way, topological modes encoded in $\boldsymbol{\beta}$ can appear in the nonlinear regime. In the fully dimerized limit ($w \to 0$), μ_k can be calculated explicitly and one finds two degenerate eigenstates at $\mu_k = g$, corresponding to the topologically protected edge modes, and $n-2$ degenerate bulk modes at $\mu_k = g \pm s$ (*SI Appendix*). The bulk eigenvectors are pairwise localized with components $(1, \pm 1)$ on one of the dimers and zero everywhere else, corresponding to a low-energy in-phase oscillation ($\mu_k = g - s$) and a high-energy antiphase oscillation ($\mu_k = g + s$) (*SI Appendix*). This implies that the dimers' dynamics near the rest state are approximately decoupled and governed by the eigenvalues $\sqrt{-g \mp s}$. If $g > s$, all modes are oscillatory, while for $g < s$, the antiphase mode becomes unstable and is not physically realizable. Armed with these analytical insights, we proceed to numerically characterize the interesting nonlinear effects that arise in ATCs. In the simulations, we can fix $g = 1$ without loss of generality, which is equivalent to dividing Eq. **2** by g and rescaling $t \to \sqrt{g}t$, $\varepsilon \to \varepsilon/\sqrt{g}$, $s \to s/g$, and $w \to w/g$.

In contrast to passive ($\varepsilon = 0$) topolectrical circuits, which remain quiescent in the bulk when initiated at the edge (Fig. 1*D*), ATCs with $\varepsilon > 0$ exhibit complex self-organization and synchronization phenomena. To explain the underlying physical mechanisms, we consider the 1D SSH ATC from Fig. 1*B* with the same initial condition as for the passive circuit in Fig. 1*D*. When one edge node of the ATC is initialized at time $t = 0$, it rapidly settles into a limit-cycle oscillation (Fig. 1 *E* and *F*), as predicted above. As it gets activated, the edge mode imparts a weak external forcing on the neighboring strongly coupled dimer. The combination of forcing and local energy input from the negative resistance drives the dimer into its low-energy state, characterized by a slow nonlinear in-phase oscillation of the dimer nodes with period $2\pi/\sqrt{g - s}$ (Fig. 1 *E* and *G*). The first bulk dimer then in turn activates the second dimer, and so on, resulting in a globally synchronized bulk state. The activation front eventually reaches the last node, where it triggers the second topological edge mode (Fig. 1*F*). The final state of the chain is a robust attractor that is self-sustained and could be used for active solitary signal transmission.

One-Dimensional Su–Schrieffer–Heeger ATC: Experimental Realization. As a first experimental demonstration of the underlying general concepts, we built a 1D four-node ATC using a Chua diode circuit as the active element (Fig. 2 *A*–*C*). The measured time series of the oscillator voltages exhibit the theoretically predicted topological edge modes and low-frequency bulk dynamics (Fig. 1). In the case of active circuits, the edge modes excite the bulk abruptly over the scale of just a single oscillation, even when corresponding passive circuits would exhibit exponential decay over a longer scale. The quantitative agreement of the experiments with theory as well as explicit circuit simulations (*SI Appendix*) confirms that Eq. **2** provides a predictive framework for ATCs—and that it is straightforward to realize active topolectrical materials with off-the-shelf components. Indeed, the example in Fig. 2 is only one of many possible ATC implementations (*SI Appendix*).

Attractor Statistics. In practice, ATCs can be actuated with a wide range of initial conditions that can select different types of stable asymptotic behaviors (Fig. 3), similar to information storage in Hopfield networks. To investigate the likelihood and characteristics of possible attractors, we used Eq. **2** to simulate an active SSH circuit with $n = 6$ nodes with nonzero initial conditions on the bulk (Fig. 3*A*). Since the edge node initial conditions become negligible in this case due to the weak edge–bulk coupling, we fixed zero initial conditions at the edges. Thus, the topological edge modes are actuated by the bulk dynamics in these simulations. Examples of low-energy and high-energy attractors with slow and fast bulk dimer oscillations, obtained with binary initial conditions in the bulk, $x_i(0) = \pm 0.1$ and $\dot{x}_i(0) = 0$, are shown in Fig. 3*A*. These attractors can be classified in terms of the relative signs of the $n_b = n - 2 = 4$ bulk voltages x_i at a fixed time. Normalizing by the sign of the first bulk oscillator, we numerically find that there exist four different stable attractors corresponding to different possible combinations of in-phase and antiphase dimer oscillations (Fig. 3 *A* and *B*).

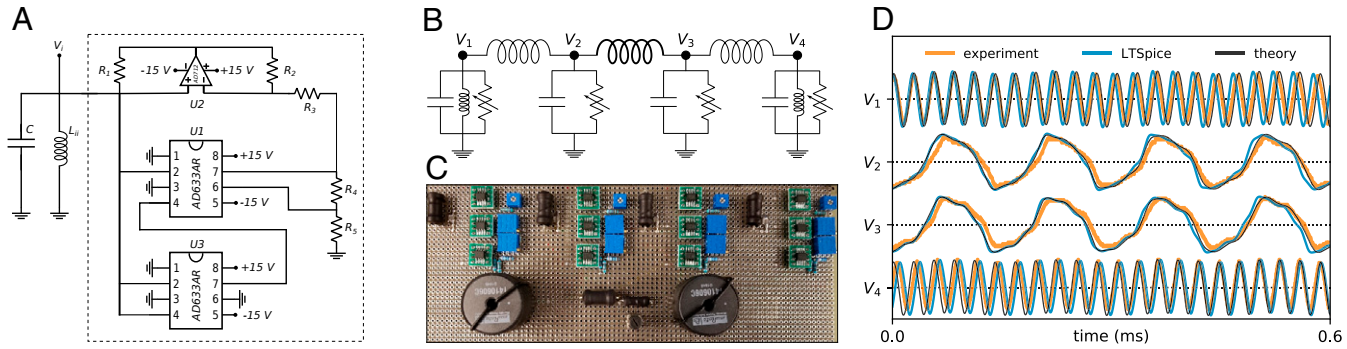

Fig. 2. Experimental realization of a 1D active topolectric circuit with four nodes. (*A*) Implementation of a single active node using a Chua diode circuit (*SI Appendix*). (*B*) Four-node active topolectrical circuit using $C = 42$ nF, $L_{12} = L_{34} = 10.5$ mH, $L_{23} = 525$ μH. To obtain the classical SSH coupling matrix Eq. **3**, no inductors were used for the bulk nodes, such that $L_{11} = L_{44} = 525$ μH. The corresponding dimensionless parameters are $s = 1.0$, $w = 0.05$, $g = 1.05$, and $\varepsilon = 0.28$. (*C*) Experimental setup on circuit board. (*D*) Experimental data (orange lines), simulations of the full circuit using LTSpice (blue lines), and theoretical simulation using Eq. **2** match. Voltages V_1 to V_4 vary between ± 6 V; in-phase initial conditions were chosen on the two bulk oscillators.

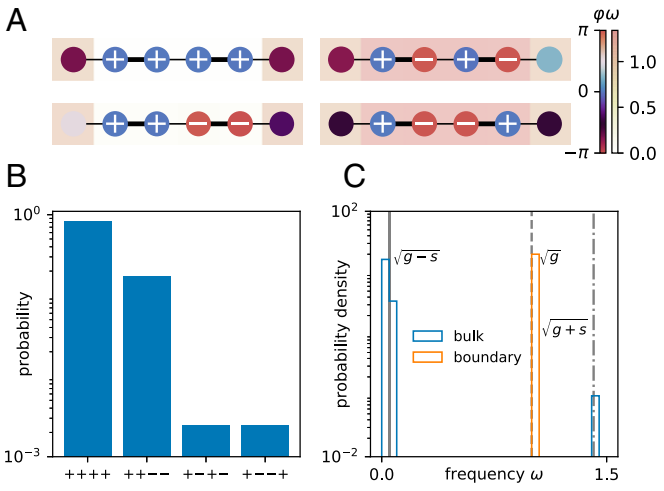

Fig. 3. Attractor statistics of a 1D ATC. (*A*) An active SSH circuit with $n = 6$ vdP nodes has four qualitatively distinct stable attractors. Circle size represents instantaneous absolute voltage $|x_i(t)|$, symbol color the phase φ, and background color the time-averaged frequency $\omega = \langle\dot{\varphi}\rangle$ of the oscillators. Two low-energy attractors exhibit in-phase dynamics of the bulk dimer nodes, and two high-energy attractors show antiphase dynamics on the bulk dimers. (*B*) Low-energy attractors are substantially more frequently realized when bulk nodes are initialized with uniformly random $x_i(0) \in [-4, 4]$ and $\dot{x}_i(0) \in [-0.4, 0.4]$. The two in-phase states are approached for $\approx 99.5\%$ of initial conditions. (*C*) Frequencies of nonlinear bulk oscillations cluster around $\sqrt{g \pm s}$ (solid/dashed-dotted line) and boundary oscillations around $\sqrt{g}$ (dashed line), as predicted by linearized theory. Simulation parameters: $g = 1$, $w = 0.003$, $s = g - w$, and $\varepsilon = 0.1$. Histograms were computed from 50,000 trajectories, integrated up to $t = 1{,}000$.

To estimate the likelihood of observing a specific attractor in experiments, we performed 50,000 simulations with randomly chosen bulk initial data. To explore a large neighborhood of the bulk limit cycle (Fig. 1*G*), initial conditions were sampled uniformly from the eight-dimensional domain $x_i(0) \in [-4, 4]$, $\dot{x}_i(0) \in [-0.4, 0.4]$. These simulations predict that, in practice, low-energy states with in-phase bulk dimers are much more likely than high-energy attractors with many antiphase dimers (Fig. 3*B*). Mixed in-phase/antiphase dimer attractors are not observed for this parameter regime. Furthermore, even though the shape of the bulk limit cycles indicates highly nonlinear relaxation dynamics (Fig. 1*G*), the numerically determined time-averaged frequencies $\langle\dot{\varphi}\rangle$, where $\varphi(t) = \arctan(\dot{x}(t)/x(t))$, agree remarkably well with the bulk oscillation frequencies $\sqrt{g \pm s}$ and boundary oscillation frequency $\sqrt{g}$ predicted by the linearized theory above (Fig. 3*C*). Based on these observations, one expects that low-energy attractors with in-phase bulk dimer dynamics will also be dominant in more complex ATCs and that their bulk and edge frequencies can be estimated from spectra of the coupling matrix $\boldsymbol{\beta}$ in the weak-coupling limit.

Experimental Realization of a 2D SSH ATC. ATC implementations become particularly powerful in $d \geq 2$ dimensions. Different types of 2D SSH lattices can be constructed by stacking 1D SSH chains and connecting them using alternating strong and weak couplings (Fig. 4). This procedure allows the realization of two essentially different topological regimes T1 and T2, which we realized in simulations and experiments (*SI Appendix*): In the T1 regime, topologically protected modes exist along two opposite edges of a finite sample (Fig. 4*A* and Movie S1), whereas in the T2 regime such modes exist on all four of the edges including the corners (Fig. 4*B* and Movie S2) (29). Because essential aspects of the dynamics are qualitatively similar for both cases, we focus our discussion on the T2 regime. In this case, one can distinguish three different groups of oscillators: corner oscillators that are only weakly coupled to their neighbors, strongly coupled vdP dimers along the edges that are similar to the 1D case, and quartets of strongly coupled vdP oscillators in the bulk (Fig. 4 *B*, *E*, *F*, and *H*). Each quartet is weakly coupled to its neighbors. Analogous to the 1D case, the linear stability of the quartets can be analyzed independently in the weak-coupling limit $w \to 0$, revealing that the lowest-frequency mode is an in-phase state $((1, 1; 1, 1))$ with period $2\pi/\sqrt{g - 2s}$ (*SI Appendix*). Similar to the 1D case, in the limit $(g - 2s) \to 0^+$, the bulk quartets collectively synchronize to the low-frequency in-phase state, avoiding mixing of bulk excitations with corners and edges (61). However, the dimers on the boundary now oscillate at a frequency lower than that of the corner nodes, because $(g - s) \to s$ as $(g - 2s) \to 0^+$. This opens the intriguing possibility of using topological protected modes to control oscillation patterns in 2D ATCs. In particular, by varying the ground inductances of each of the nodes one can control frequencies of each of the corner nodes, edge dimers, and bulk quartets (*SI Appendix*).

Initializing the 2D active SSH circuits with a nonzero voltage at one of the corner nodes, one finds that essential qualitative features of the dynamics seen in 1D ATCs carry over to the 2D case. In particular, the boundary nodes belonging to topologically protected corner modes and edge modes become activated one after the other and settle down in their respective vdP limit cycles. Similarly, in the bulk, quartets of strongly coupled oscillators synchronize. Because the in-phase state is the lowest-energy attractor above the quiescent state, the bulk synchronizes in a global in-phase pattern (Fig. 4 *B*–*D*). Thus, in both 1D and 2D ATCs, topologically protected edge modes become activated via self-sustained oscillations, while the bulk dynamics are almost decoupled, leading to synchronization.

Robustness of Self-Excited Edge Modes. Crucially, this ATC self-organization principle remains valid in the presence of lattice defects, demonstrating that topological protection phenomena can survive in the nonlinear regime $\varepsilon > 0$ (Fig. 4 *C*, *D*, and *I*). Introducing an edge defect in a passive $(\varepsilon = 0)$ 2D SSH grid by removing a few unit cells does not affect the localized nature of the edge state, which now wraps around the defect due to topological protection from the linear coupling (Fig. 4 *C* and *I*). Self-sustained oscillations in nonlinear active $(\varepsilon > 0)$ circuits inherit this topological protection globally: In the presence of edge defects, all boundary nodes continue to oscillate at a high nonzero frequency while bulk quartets synchronize at low frequency (Fig. 4 *B* and *E* and Movie S3). Similarly, bulk defects also lead to localized nonlinear edge oscillations (Fig. 4*D* and Movie S4). These results show that the SSH network topology can be used to precisely control the individual and collective behavior of coupled nonlinear oscillators. Furthermore, the above ideas can be extended to achieve control of active traveling-wave patterns by means of nontopological defects. By strategically placing bulk defects, one can guide the self-organization of active wave patterns that can be initiated from a single corner node (*SI Appendix* and Movie S5). More broadly, these results open a path toward the inverse design of functionalized active topolectrical networks (62) in the future.

General Design Rules for ATCs. The above analysis, combined with insights from earlier studies (4, 5, 26, 44), suggests general design principles for ATCs, by additively combining local Rayleigh-type activity with suitably designed conservative node-coupling interactions (62, 63). Previous investigations (5, 44, 62, 64) showed that, in the low-to-moderate activity regime, nonlinear Rayleigh-type driving mechanisms often select dynamical attractors that reflect the mode structure of the corresponding nondriven system. In these cases, the nonlinear driving

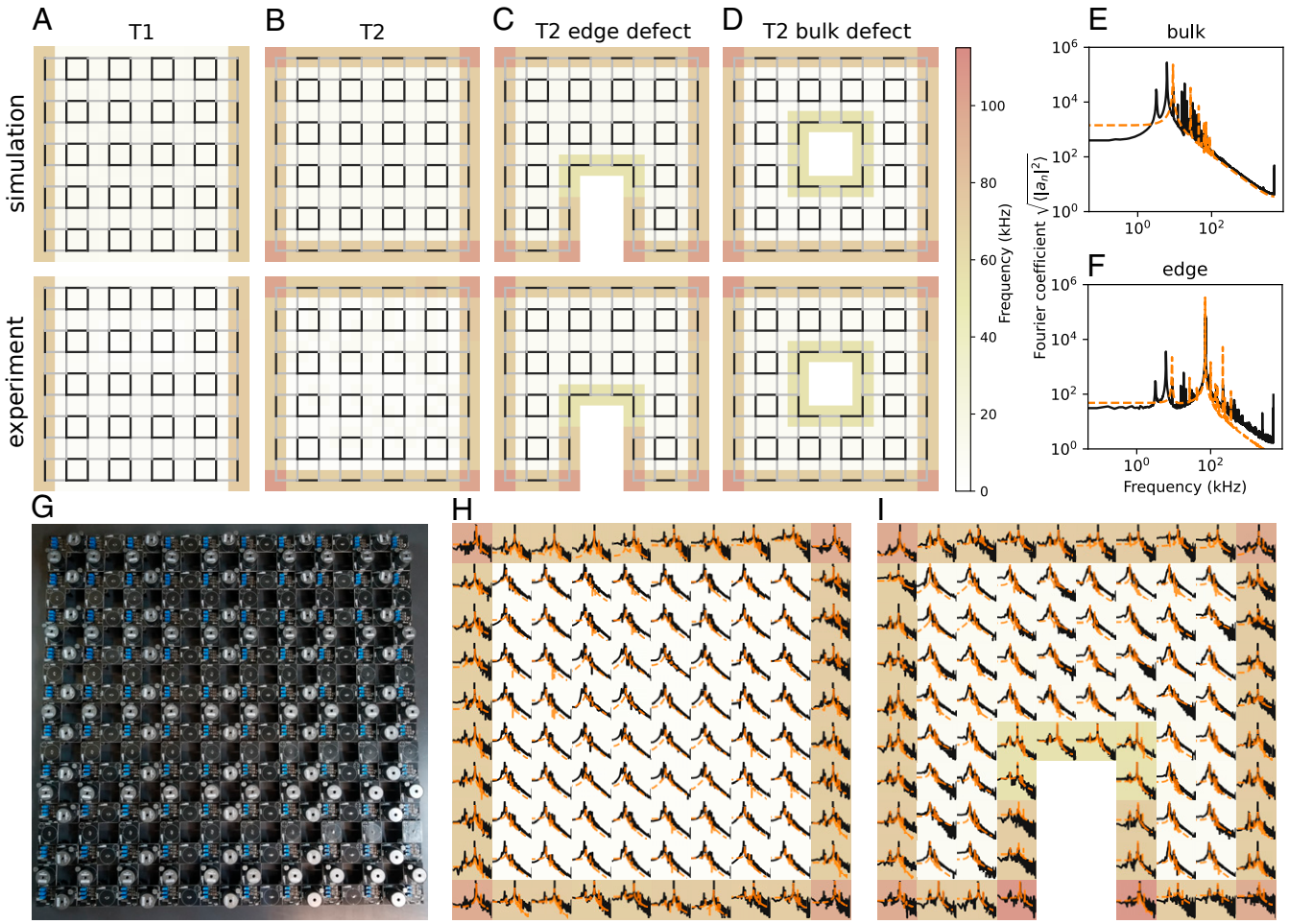

Fig. 4. Self-organized, self-sustained nonlinear oscillations in 2D ATCs recapitulate topological edge mode phenomena in simulations of Eq. **2** and corresponding experiments based on Chua diode circuits. (*A* and *B*) Frequency patterns measured in simulations and experiments confirm the self-excitation of the topological edge mode T1 regime (*A*) and the topological corner-edge mode T2 regime (*B*), respectively. Line width indicates inductive coupling strength, and background color shows dominant frequency obtained from Fourier spectra of the individual oscillator time series. (*C* and *D*) In the presence of edge defects (*C*) or bulk defects (*D*), the high-frequency dynamics remain robustly localized along the boundaries. (*E* and *F*) Root-mean-square Fourier spectra measured in experiments (black) and simulations (orange) obtained by averaging over all bulk and edge oscillators, respectively, for the T2 networks (*B* and *H*). The peak frequencies indicate slow bulk node oscillations and fast edge node oscillations. (*G*) Experimental ATC setup from which the data shown in *A*–*D*, *H*, and *I* were acquired. An alternative experimental 2D ATC realization is given in *SI Appendix*. (*H* and *I*) Fourier power spectra for the individual oscillator voltage time series measured in experiments (*B* and *C*, *Bottom*; black) and corresponding simulations (*B* and *C*, *Top*; orange) of Eq. **2**. Background colors show peak frequencies using the same color scale as in *A*–*D*. Axis scales of the individual spectra are equal to those in *E* and *F*. Experiments and simulations were performed for grounding capacitances $C = 42$ nF, bulk inductances $L_w = 13.3$ mH, and $L_s = 122\ \mu H$ and nonlinear resistance parameters $\alpha = 2.5\ \mathrm{m}\Omega$, $\gamma = 90.7\ \mu\Omega \cdot \mathrm{V}^{-2}$. Despite its minimal generic character, Eq. **2** correctly predicts the experimentally observed edge mode phenomenology.

determines the mode amplitudes while quadratic expansions of the interaction potentials determine the mode characteristics. Conversely, recent studies (26, 62) have demonstrated that, by designing the linear response of nonlinear mechanical networks, one can control the spectral features, such as band gaps, of self-excited waves in the presence of activity. Building on this general idea, the above experimental realizations of ATCs provide an extension to lattices with structured linear couplings that support self-sustained topologically protected phononic excitations. An interesting direction for future research is the design and implementation of autonomous electrical circuits that combine structured nonlinear (e.g., Toda-like) (4, 36) couplings with nonlinear activity, which can be expected to support self-sustained solitonic (4, 44) edge excitations.

Conclusion

Active topolectrical circuits promise a wide range of applications, from active wave guides to autonomous electronic circuits with topologically protected functionalities. The framework developed here can be integrated with recently developed methods for the inverse design of network-based metamaterial structures (63, 65), to optimize and tailor the node couplings and transmission properties. The close agreement with our 1D and 2D experiments suggests that the generic ATC model from Eq. **2** provides a useful theoretical basis for the implementation of more complex ATCs. For example, by designing the coupling matrix β such that the associated dynamical matrix possesses chiral (50) or other symmetries, one can realize different topological phases by utilizing generic vdP-type nonlinearities. Another intriguing prospect is the possibility of creating and studying electronic metamaterials with effective dimensions $d > 3$ that appear to be difficult to access otherwise. Beyond man-made devices, the above results suggest that it would be interesting to explore whether active biological circuits (66, 67) may use topological coupling regimes to facilitate robust signal transport and information storage.

Materials and Methods

Nondimensionalization of Variables and Parameters. Given a lattice circuit, we state the equations of its voltage dynamics using Kirchoff's laws as follows:

$$C\ddot{V}_i - (\alpha - 3\gamma V_i^2)\dot{V}_i + \left(\frac{1}{L_{ii}} + \sum_{\substack{k \\ k\neq i}} \frac{1}{L_{ik}}\right) V_i - \sum_{\substack{j \\ j\neq i}} \frac{V_j}{L_{ij}} = 0, \qquad [4]$$

where V_i is the voltage, C is the capacitance, L_{ii} is the ground inductance, and α and γ are the vdP parameters of the oscillator at node i, while L_{ij} are the coupling inductances between nodes i and j. The coupling inductances can be either of L_w or L_s, where the subscripts w and s stand for weak and strong coupling, respectively ($1/L_w < 1/L_s$). Note that for nodes i and k that are not connected, we have $1/L_{ik} = 0$.

We introduce a voltage scale $V_i = V_0\hat{V}_i$ and a time scale $t = \tau\hat{t}$, and we scale all the inductances by the smallest inductance, say L_0, to get $L_{ij} = L_0\hat{L}_{ij}$ for all i and j. For τ, we use the natural time scale of an oscillator such that $\tau = \sqrt{L_0C}$, and the voltage scale is given by $V_0 = \sqrt{\alpha/(3\gamma)}$. The dimensionless dynamics are then given by Eq. **2**, where $\dot{V}_i = x_i$, $\varepsilon = \alpha\sqrt{L_0/C}$, $\beta_{ij} = -L_0/L_{ij}$ for $i \neq j$, and $\beta_{ii} = L_0(1/L_{ii} + \sum_{\substack{k \\ k\neq i}} 1/L_{ik})$.

In Eq. **3**, the weak and strong couplings are given by $w = L_0/L_w$ and $s = L_0/L_s$, respectively, while L_{ii} are chosen such that $g = L_0(1/L_{ii} + \sum_{\substack{k \\ k\neq i}} 1/L_{ik})$ for each i. The coupling matrix can be generalized by replacing g by g_i.

Circuit Implementation. A detailed description of the two circuit designs based on Chua's diode (68) and nonlinear resistors (4), respectively, and the component parameters used in our experiments is given in *SI Appendix*.

Data Availability. All study data are included in this article and/or *SI Appendix*.

ACKNOWLEDGMENTS. J.D. thanks the Isaac Newton Institute for Mathematical Sciences for support and hospitality during the program "The Mathematical Design of New Materials" (supported by Engineering and Physical Sciences Research Council Grant EP/R014604/1) when work on this paper was undertaken. This work was supported by a James S. McDonnell Foundation Complex Systems Scholar Award (to J.D.), the Massachusetts Institute of Technology Solomon Buchsbaum Research Fund (J.D.), and the Robert E. Collins Distinguished Scholar Fund (J.D.). The work in Würzburg is funded by the Deutsche Forschungsgemeinschaft (German Research Foundation) through Project ID 258499086-SFB 1170 and through the Würzburg–Dresden Cluster of Excellence on Complexity and Topology in Quantum Matter—*ct.qmat* Project ID 39085490-EXC 2147.

1. R. FitzHugh, Mathematical models of threshold phenomena in the nerve membrane. *Bull. Math. Biophys.* **17**, 257–278 (1955).
2. J. Nagumo, S. Arimoto, S. Yoshizawa, An active pulse transmission line simulating nerve axon. *Proc. IRE* **50**, 2061–2070 (1962).
3. E. M. Izhikevich, Dynamical systems in neuroscience: The geometry of excitability and bursting (MIT Press, 2007).
4. V. A. Makarov, E. del Río, W. Ebeling, M. G. Velarde, Dissipative Toda-Rayleigh lattice and its oscillatory modes. *Phys. Rev. E* **64**, 036601 (2001).
5. E. del Río, V. A. Makarov, M. G. Velarde, W. Ebeling, Mode transitions and wave propagation in a driven-dissipative Toda-Rayleigh ring. *Phys. Rev. E Stat. Nonlin. Soft Matter Phys.* **67**, 056208 (2003).
6. S. Weimann *et al*., Topologically protected bound states in photonic parity-time-symmetric crystals. *Nat. Mater.* **16**, 433–438 (2017).
7. A. B. Khanikaev *et al*., Photonic topological insulators. *Nat. Mater.* **12**, 233–239 (2013).
8. Y. Lumer, Y. Plotnik, M. C. Rechtsman, M. Segev, Self-localized states in photonic topological insulators. *Phys. Rev. Lett.* **111**, 243905 (2013).
9. J. Noh *et al*., Topological protection of photonic mid-gap defect modes. *Nat. Photonics* **12**, 408–415 (2018).
10. Z. Yang *et al*., Topological acoustics. *Phys. Rev. Lett.* **114**, 114301 (2015).
11. H. Xue, Y. Yang, F. Gao, Y. Chong, B. Zhang, Acoustic higher-order topological insulator on a kagome lattice. *Nat. Mater.* **18**, 108–112 (2019).
12. X. Ni, M. Weiner, A. Alù, A. B. Khanikaev, Observation of bulk polarization transitions and higher-order embedded topological eigenstates for sound. arXiv [Preprint] (2018). https://arxiv.org/abs/1807.00896 (Accessed 23 July 2021).
13. C. Kane, T. Lubensky, Topological boundary modes in isostatic lattices. *Nat. Phys.* **10**, 39 (2014).
14. S. D. Huber, Topological mechanics. *Nat. Phys.* **12**, 621–623 (2016).
15. L. M. Nash *et al*., Topological mechanics of gyroscopic metamaterials. *Proc. Natl. Acad. Sci. U.S.A.* **112**, 14495–14500 (2015).
16. B. G. Chen, N. Upadhyaya, V. Vitelli, Nonlinear conduction via solitons in a topological mechanical insulator. *Proc. Natl. Acad. Sci. U.S.A.* **111**, 13004–13009 (2014).
17. M. Z. Hasan, C. L. Kane, Colloquium: Topological insulators. *Rev. Mod. Phys.* **82**, 3045 (2010).
18. B. A. Bernevig, T. L. Hughes, S. C. Zhang, Quantum spin Hall effect and topological phase transition in HgTe quantum wells. *Science* **314**, 1757–1761 (2006).
19. L. Fu, C. L. Kane, E. J. Mele, Topological insulators in three dimensions. *Phys. Rev. Lett.* **98**, 106803 (2007).
20. D. Hsieh *et al*., A topological Dirac insulator in a quantum spin Hall phase. *Nature* **452**, 970–974 (2008).
21. J. E. Moore, L. Balents, Topological invariants of time-reversal-invariant band structures. *Phys. Rev. B Condens. Matter Mater. Phys.* **75**, 121306 (2007).
22. X. Qi, S. C. Zhang, Topological insulators and superconductors. *Rev. Mod. Phys.* **83**, 1057 (2011).
23. S. N. Kempkes *et al*., Robust zero-energy modes in an electronic higher-order topological insulator. *Nat. Mater.* **18**, 1292–1297 (2019).
24. C. W. Peterson, W. A. Benalcazar, T. L. Hughes, G. Bahl, A quantized microwave quadrupole insulator with topologically protected corner states. *Nature* **555**, 346–350 (2018).
25. A. Souslov, B. C. van Zuiden, D. Bartolo, V. Vitelli, Topological sound in active-liquid metamaterials. *Nat. Phys.* **13**, 1091–1094 (2017).
26. F. G. Woodhouse, H. Ronellenfitsch, J. Dunkel, Autonomous actuation of zero modes in mechanical networks far from equilibrium. *Phys. Rev. Lett.* **121**, 178001 (2018).
27. S. Shankar, A. Souslov, M. J. Bowick, M. C. Marchetti, V. Vitelli, Topological active matter. arXiv [Preprint] (2020). https://arxiv.org/abs/2010.00364 (Accessed 23 July 2021).
28. C. H. Lee *et al*., Topolectrical circuits. *Nat. Commun.* **1**, 39 (2018).
29. S. Imhof *et al*., Topolectrical-circuit realization of topological corner modes. *Nat. Phys.* **14**, 925 (2018).
30. T. Helbig *et al*., Band structure engineering and reconstruction in electric circuit networks. *Phys. Rev. B* **99**, 161114 (2019).
31. J. Ningyuan, C. Owens, A. Sommer, D. Schuster, J. Simon, Time-and site-resolved dynamics in a topological circuit. *Phys. Rev. X* **5**, 021031 (2015).
32. V. V. Albert, L. I. Glazman, L. Jiang, Topological properties of linear circuit lattices. *Phys. Rev. Lett.* **114**, 173902 (2015).
33. K. Luo, R. Yu, H. Weng, Topological nodal states in circuit lattice. *Research (Wash. D C)* **2018**, 6793752 (2018).
34. M. Ezawa, Higher-order topological electric circuits and topological corner resonance on the breathing kagome and pyrochlore lattices. *Phys. Rev. B* **98**, 201402 (2018).
35. Y. Hadad, J. C. Soric, A. B. Khanikaev, A. Alù, Self-induced topological protection in nonlinear circuit arrays. *Nat. Electron.* **1**, 178–182 (2018).
36. M. Ezawa, Topological Toda lattice and nonlinear bulk-edge correspondence. arXiv [Preprint] (2021). https://arxiv.org/abs/2105.10851 (Accessed 23 July 2021).
37. S. Iwamoto, Y. Ota, Y. Arakawa, Recent progress in topological waveguides and nanocavities in a semiconductor photonic crystal platform (invited). *Opt. Mater. Express.* **11**, 319–337 (2021).
38. G. Harari *et al*., Topological insulator laser: Theory. *Science* **359**, eaar4003 (2018).
39. M. A. Bandres *et al*., Topological insulator laser: Experiments. *Science* **359**, eaar4005 (2018).
40. Y. Wang, L. J. Lang, C. H. Lee, B. Zhang, Y. D. Chong, Topologically enhanced harmonic generation in a nonlinear transmission line metamaterial. *Nat. Commun.* **10**, 1102 (2019).
41. S. Sayed, S. Hong, S. Datta, Transmission-line model for materials with spin-momentum locking. *Phys. Rev. Appl.* **10**, 054044 (2018).
42. T. Jiang *et al*., Experimental demonstration of angular momentum-dependent topological transport using a transmission line network. *Nat. Commun.* **10**, 434 (2019).
43. A. K. Iyer, G. V. Eleftheriades, A three-dimensional isotropic transmission-line metamaterial topology for free-space excitation. *Appl. Phys. Lett.* **92**, 261106 (2008).
44. A. Forrow, F. G. Woodhouse, J. Dunkel, Mode selection in compressible active flow networks. *Phys. Rev. Lett.* **119**, 028102 (2017).
45. F. G. Woodhouse, A. Forrow, J. B. Fawcett, J. Dunkel, Stochastic cycle selection in active flow networks. *Proc. Natl. Acad. Sci. U.S.A.* **113**, 8200–8205 (2016).
46. J. G. Nicholls *et al*., *From Neuron to Brain* (Sinauer Associates, 2012).
47. B. W. Connors, M. A. Long, Electrical synapses in the mammalian brain. *Annu. Rev. Neurosci.* **27**, 393–418 (2004).
48. B. B. Johnson, S. V. Dhople, A. O. Hamadeh, P. T. Krein, Synchronization of nonlinear oscillators in an lti electrical power network. *IEEE Trans. Circuits Syst. I Regul. Pap.* **61**, 834–844 (2014).
49. I. Gottlieb, *Practical Oscillator Handbook* (Elsevier Science, 1997).
50. T. Hofmann, T. Helbig, C. H. Lee, M. Greiter, R. Thomale, Chiral voltage propagation and calibration in a topolectrical chern circuit. *Phys. Rev. Lett.* **122**, 247702 (2019).
51. D. Dobrykh, A. Yulin, A. Slobozhanyuk, A. Poddubny, Y. S. Kivshar, Observation and control of nonlinear electromagnetic topological edge states. *Phys. Rev. Lett.* **121**, 163901 (2018).
52. T. Morimoto, N. Nagaosa, Topological nature of nonlinear optical effects in solids. *Sci. Adv.* **2**, e1501524 (2016).
53. T. Shi, H. J. Kimble, J. I. Cirac, Topological phenomena in classical optical networks. *Proc. Natl. Acad. Sci. U.S.A.* **114**, E8967–E8976 (2017).
54. J. J. Stoker, *Nonlinear Vibrations in Mechanical and Electrical Systems* (Interscience Publishers, New York, NY, 1950), vol. 2.
55. P. Romanczuk, M. Bär, W. Ebeling, B. Lindner, L. Schimansky-Geier, Active Brownian particles. *Eur. Phys. J. Spec. Top.* **202**, 1–162 (2012).
56. W. Su, J. Schrieffer, A. J. Heeger, Solitons in polyacetylene. *Phys. Rev. Lett.* **42**, 1698 (1979).

57. J. K. Asbóth, L. Oroszlány, A. Pályi, *A Short Course on Topological Insulators* (Springer, 2016).
58. D. Storti, R. Rand, Dynamics of two strongly coupled van der Pol oscillators. *Int. J. Non-linear Mech.* **17**, 143–152 (1982).
59. S. Wirkus, R. Rand, The dynamics of two coupled van der Pol oscillators with delay coupling. *Nonlinear Dyn.* **30**, 205–221 (2002).
60. S. H. Strogatz, *Nonlinear Dynamics and Chaos: With Applications to Physics, Biology, Chemistry, and Engineering* (CRC Press, 2018).
61. W. A. Benalcazar, A. Cerjan, Bound states in the continuum of higher-order topological insulators. *Phys. Rev. B* **101**, 161116 (2020).
62. H. Ronellenfitsch, J. Dunkel, "Spectral design of active mechanical and electrical metamaterials" in *2020 Fourteenth International Congress on Artificial Materials for Novel Wave Phenomena (Metamaterials)* (IEEE, New York, NY, 2020), pp. 270–272.
63. H. Ronellenfitsch, N. Stoop, J. Yu, A. Forrow, J. Dunkel, Inverse design of discrete mechanical metamaterials. *Phys. Rev. Mater.* **3**, 095201 (2019).
64. J. Dunkel, W. Ebeling, U. Erdmann, V. A. Makarov, Coherent motions and clusters in a dissipative Morse ring chain. *Int. J. Bifurcat. Chaos* **12**, 2359–2377 (2002).
65. A. Forrow, F. G. Woodhouse, J. Dunkel, Functional control of network dynamics using designed Laplacian spectra. *Phys. Rev. X* **8**, 041043 (2018).
66. A. Murugan, S. Vaikuntanathan, Topologically protected modes in non-equilibrium stochastic systems. *Nat. Commun.* **8**, 13881 (2017).
67. J. Knebel, P. M. Geiger, E. Frey, Topological phase transition in coupled rock-paper-scissors cycles. *Phys. Rev. Lett.* **125**, 258301 (2020).
68. G. Q. Zhong, Implementation of Chua's circuit with a cubic nonlinearity. *IEEE Trans. Circuits Syst-I* **41**, 934–941 (1994).